J. Mech. Phys. Solids 204 (2025) 106301

Contents lists available at ScienceDirect

Journal of the Mechanics and Physics of Solids

journal homepage: www.elsevier.com/locate/jmps

Wrinkling instability of 3D auxetic bilayers in tension ☆

Sairam Pamulaparthi Venkata [a,b,*,1], Yuxin Fu [c,1], Yibin Fu [d], Hooman Danesh [e], Michel Destrade [a,f], Valentina Balbi [a]

[a] School of Mathematical and Statistical Sciences, University of Galway, University Road, Galway, H91 TK33, Ireland
[b] Department of Anatomy and Regenerative Medicine, Royal College of Surgeons in Ireland, 123 St Stephen's Green, Dublin 2, D02 YN77, Ireland
[c] Department of Mechanics, Tianjin University, Tianjin 300072, People's Republic of China
[d] School of Computer Science and Mathematics, Keele University, Staffs ST5 5BG, United Kingdom
[e] Institute of Applied Mechanics, RWTH Aachen University, Mies-van-der-Rohe-Str.1, Aachen, 52074, Germany
[f] Key Laboratory of Soft Machines and Smart Devices of Zhejiang Province and Department of Engineering Mechanics, Zhejiang University, Hangzhou 310027, People's Republic of China

ARTICLE INFO

Keywords:
Auxetic structures
Bilayers
Tension instability
Wrinkles
Inverse analysis
Hyperelasticity
Surface instabilities

ABSTRACT

Bilayers, soft substrates coated with stiff films, are commonly found in nature, with examples including skin tissue, vesicles, and organ membranes. They exhibit different types of instabilities when subjected to compression, depending on the contrast in material properties between the two components. In this work, we unravel the mechanisms behind wrinkling instabilities in auxetic bilayer systems under uniaxial tension. We find that a soft bilayer in tension can experience significant lateral contraction, and with sufficient contrast in Poisson ratios, compressive stresses may induce wrinkles aligned with the tensile direction. We analytically model the onset of wrinkles and validate our predictions using Finite Element simulations in ABAQUS. Our findings reveal that wrinkles may occur when the Poisson ratio of the substrate is greater than that of the film. As the two Poisson ratios converge to a common value, the critical stretch for instability shoots up rapidly and the wrinkles disappear. We also confirm these results through asymptotic analysis. Using inverse analysis, we design film microstructures to achieve desired effective Poisson ratios and further validate the effective properties with the Finite Element code FEAP. We show that the critical stretch ratio for buckling in auxetic structures with microstructural patterns is in strong agreement with the homogenized model predictions. The proposed method has significant potential for controlling surface patterns in auxetic skin grafts and hydrogel organ patches under mechanical loads. Moreover, the asymptotic expressions for compressible bilayers developed in this work can also be applied under finite strain for buckling-based metrology.

1. Introduction

Auxetics, materials with negative Poisson's ratio, expand in all directions under uniaxial tension. For 3D isotropic materials with auxetic behavior, which obey the pointwise energy stability criterion, the theoretical value of Poisson's ratio ranges between −1 and 0.5 (Timoshenko, 1983).

☆ This research project is funded by the XS-META ITN: Marie Skłodowska-Curie European Actions (Grant Agreement No. 956401).
* Corresponding author at: School of Mathematical and Statistical Sciences, University of Galway, University Road, Galway, H91 TK33, Ireland.
E-mail address: sairampamulaparthive@rcsi.com (S. Pamulaparthi Venkata).
[1] These authors contributed equally to this work.

https://doi.org/10.1016/j.jmps.2025.106301
Received 31 March 2025; Received in revised form 19 July 2025; Accepted 20 July 2025
Available online 31 July 2025

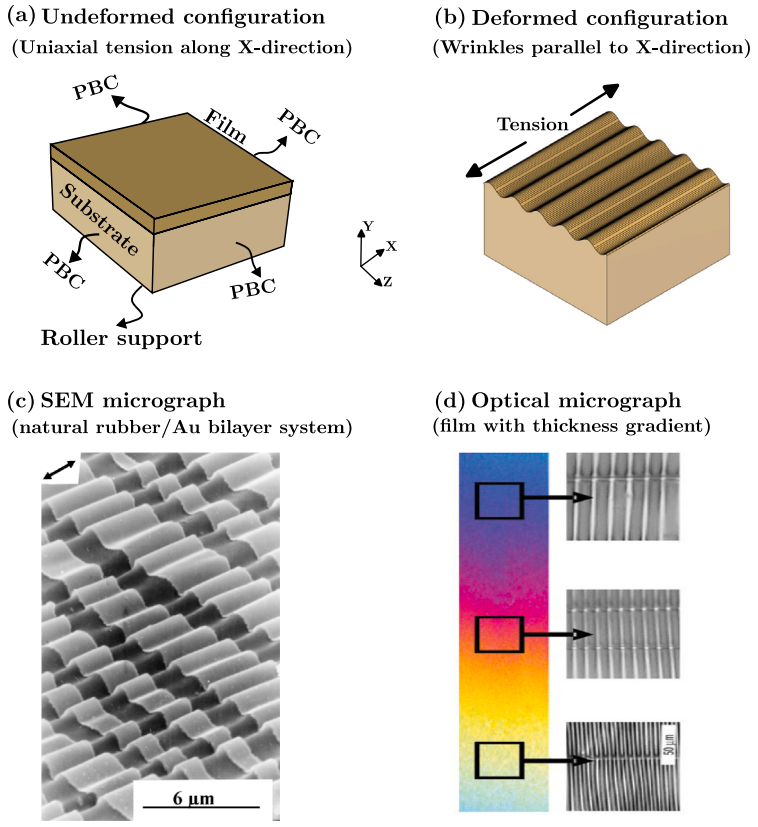

Fig. 1. (a) Undeformed and (b) deformed configurations of a 3D bilayer system with periodic boundary conditions (PBCs) in the lateral directions. The system is infinite in the $X-$ and $Z-$directions and is under uniaxial tension along the $X-$direction. The analysis shows that eventually, (b) wrinkles develop parallel to the $X-$direction, provided there is enough contrast between the constitutive parameters of the materials. (c) Image obtained using Scanning Electron Microscope (SEM) on a natural rubber substrate coated with a gold film, when elongated to 50% strain at room temperature (Volynskii et al., 2000). An inset with an arrow shows the direction of elongation. Bright and dark bands represent the buckled gold film layer and the rubber showing through cracks in the stretched film, respectively. (d) Optical micrograph of a Polystyrene (PS) film layer on a silicon wafer with decreasing thickness from top to bottom is shown in the left panel. The corresponding wrinkles exhibit decreasing wavelengths in the right panel, when the PS films are attached to a Polydimethylsiloxane (PDMS) substrate and elongated to induce buckling (Stafford et al., 2004).

Advancements in additive and subtractive manufacturing (Mueller et al., 2013; Sun et al., 2017), combined with extensive research on negative Poisson ratio materials, have bridged the gap between theoretical models and practical applications of auxetics in diverse fields. Early studies on ferromagnetic films identified a negative Poisson ratio behavior that decayed with time (Popereka and Balagurov, 1970), while subsequent work established its theoretical existence in crystalline structures (Milstein and Huang, 1979). Lakes (1987) experimentally demonstrated the auxetic behavior of open-cell polyurethane foams with tailored microstructures using thermo-mechanical treatments, and Wojciechowski and Brańka (1989) used molecular simulations to explore auxetic behavior in two-dimensional isotropic systems. Advances in material design have extended the use of auxetic properties to polymer foams, wrestling mats and aircraft sandwich panels (Lakes, 1993). Recent breakthroughs in biomedical engineering have introduced auxetic materials for medical implants, including negative Poisson ratio stents for low flexural rigidity and high circumferential strength (Dolla et al., 2006), meta-implants for improved load distribution in hip replacements (Kolken et al., 2018), and hydrogel-based organ patches that adapt to dynamic tissue mechanics (Chansoria et al., 2022).

Bilayers composed of compliant substrates coated with thin stiff films are commonly found in nature; for example, skin tissue consists of a thin, stiff epidermal layer attached to a thick, soft dermis. When subject to mechanical loads, bilayer systems can exhibit surface patterns through wrinkles. This instability phenomenon has found a wide range of applications in optical sensors (Bowden et al., 1998), novel flexible electronics (Wagner et al., 2004; Khang et al., 2006; Zhang et al., 2019), tunable phase gratings (Harrison et al., 2004), buckling-based metrology (Stafford et al., 2004; Huang et al., 2007), surface wetting (Lin and Yang, 2009), and buckling-related applications in soft matter (Crosby, 2010).

Historically, instability analysis in elastic half-spaces gained prominence through the seminal works of Biot and Taylor (1957), Biot (1963) and Allen (1969a). Dorris and Nemat-Nasser (1980) studied instabilities in bilayer systems with different material combinations of elastic and inelastic film–substrate layers. Shield et al. (1994) conducted a linear buckling analysis of a stiff layer bonded to an isotropic, elastic half-space using first-order perturbation analysis and compared the results to approximate solutions obtained via beam theory for the coating. The first weakly nonlinear analysis was conducted by Cai and Fu (1999) who found that

there existed a critical stiffness ratio at which the bifurcation changes character (from being supercritical to subcritical). Building on Gurtin–Murdoch theory (Gurtin and Ian Murdoch, 1975; Gurtin and Ian Murdoch, 1978), Steigmann and Ogden (1997) developed an incremental bifurcation theory for planar deformations of coated elastic solids with boundary elasticity.

Numerous studies have examined compression-induced surface instabilities in bilayers, driven by thermo-mechanical treatments. Experiments revealed surface instabilities, where thermal contraction of the substrate caused buckling in metal films (Bowden et al., 1998). Similarly, in metal-elastomer bilayers, thermal expansion mismatch during cooling induced equi-biaxial compression, leading to herringbone wrinkles (Chen and Hutchinson, 2004). Refined models demonstrated that wrinkles evolve into stripes, labyrinths, or herringbones, depending on the anisotropy of the membrane force (Huang et al., 2005). Choi et al. (2007) demonstrated that silicon nanomembranes on pre-strained elastomeric substrates form 2D wavy structures under uniaxial and biaxial strains, offering potential for stretchable electronics. Auguste et al. (2014) reported that an applied pre-tension in the substrate leads to the stabilization of wrinkles, while a pre-compression leads to the emergence of chaotic surface morphologies in thin coating films.

A finite deformation buckling theory was developed to describe the strain-dependent wavelength of wrinkles by Song et al. (2008). Hong et al. (2009) found that creasing in bent elastomers occurs at a lower critical strain than the Biot prediction, which aligns with experiments. Huang et al. (2017) showed that surface instabilities in 2D bilayers under compression depend on the Poisson ratio of the substrate, occurring at smaller strains in incompressible substrates than in auxetics. Cutolo et al. (2020) experimentally investigated the evolution of wrinkles in thin metal films bonded to substrates with 3D periodic surface structures. Material anisotropy and loading biaxiality influence wrinkling evolution in orthotropic films bound to compliant substrates, with phase diagrams revealing various post-buckling surface patterns, including stripes, checkerboard, and herringbone modes (Yin et al., 2018).

The formation of these surface patterns is controlled by different parameters, such as the contrast in material properties (Cai and Fu, 1999; Efimenko et al., 2005), differential growth (Goriely and Ben Amar, 2005), film-to-substrate thickness ratio (Stafford et al., 2005; Li et al., 2019), initial imperfections (Cao and Hutchinson, 2012a), nonlinearity of the substrate (Hutchinson, 2013; Brau et al., 2013; Zhuo and Zhang, 2015), curvature (Stoop et al., 2015), applied prestretch (Cao and Hutchinson, 2012b; Cai and Fu, 2019), origin of compression (Andres et al., 2018), interfacial mechanics (Bigoni et al., 2018; Bakiler and Javili, 2023), etc.

The onset of wrinkles on the surface of a solid under applied tension is rarely studied beyond the linear elastic framework (Nikravesh et al., 2019b), although they have been observed experimentally under large strains (Volynskii et al., 2000; Stafford et al., 2004), see Fig. 1 of illustrations and examples. In this paper, we conduct a linear buckling analysis of 3D hyperelastic thin stiff films on semi-infinite compliant substrates, including auxetics, under tension and large strains, addressing a gap in the literature, which has, so far, primarily focused on compression.

To conduct this investigation, we develop a semi-analytical approach in Mathematica (Wolfram Research Inc., 2022) to predict the onset of wrinkles in bilayers under uniaxial tension. We also create a UHYPER subroutine in FORTRAN to implement appropriate constitutive models in ABAQUS (ABAQUS Inc., 2019), and use custom Python scripts to simulate wrinkling in compressible bilayers with periodic boundary conditions using Finite element (FE) analysis.

Key novelties include (i) Deriving asymptotic expressions for the critical stretch ratios and wavenumber of wrinkling, applicable under finite strains and relevant for buckling-based metrology; (ii) Demonstrating that wrinkles occur only when the Poisson ratio of the substrate exceeds that of the film (as the Poisson ratios converge, the critical stretch for the instability increases sharply, causing the wrinkles to disappear). (iii) Validating the semi-analytical approach and asymptotic expressions with detailed FE simulations; (iv) Achieving targeted effective Poisson ratios in the film by altering its microstructure with an inverse design approach, and finding that the critical stretch ratio for auxetic structures with microstructural patterns aligns closely with the predictions of the homogenized models.

The paper is structured as follows. Section 2 presents the theoretical background, including the semi-analytical method, the derivation of asymptotic expressions, and an overview of the homogenization and inverse design analyses. Section 3 describes the computational approach, where we implement the Blatz–Ko strain energy model in a user-defined subroutine (UHYPER) for ABAQUS and perform buckling analysis of three-dimensional bilayer systems. We also investigate the buckling behavior of bilayers with auxetic film microstructures and compare the results with those obtained from homogenized models. Finally, Section 4 summarizes the key findings and outlines the directions for future research.

2. Theoretical framework

2.1. 3D bilayer system in tension

We consider 3D bilayer systems with a thin stiff film perfectly bonded to a semi-infinite compliant substrate, see Fig. 1(a,b). Under a uniaxial tension applied along the X-direction, the bilayer is intuitively expected to eventually develop wrinkles aligned with that direction, as shown in Fig. 1(b), provided compressive stresses develop along the Z-direction due to a sufficient Poisson ratio contrast.

To explore the influence of material properties on this wrinkling behavior, we analyze cases where both the film and substrate exhibit either auxetic or conventional mechanical responses. Auxetic materials, characterized by a negative Poisson ratio, exhibit high compressibility and are distinctly different from nearly incompressible materials with a Poisson ratio close to 0.5.

Earlier studies have employed continuum hyperelastic models derived from the Blatz–Ko strain energy function (Blatz and Ko, 1962) to describe auxetic behavior, as they capture the mechanical response of materials with negative Poisson ratios, although with certain limitations (Crespo and Montáns, 2018). For example, Ciambella and Saccomandi (2014) employed the Blatz–Ko model to

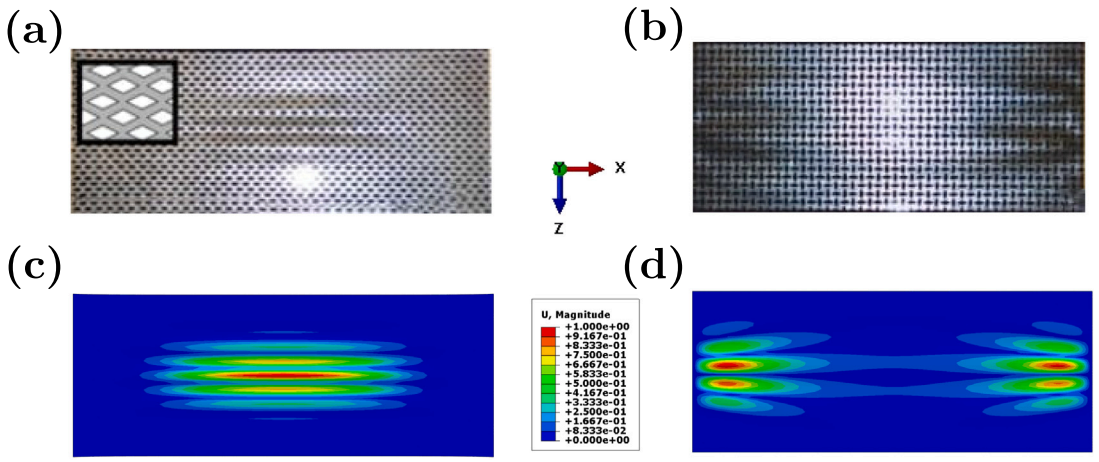

Fig. 2. Comparison of wrinkling profiles in thin conventional and auxetic sheets. Top row: Thin acetate sheets under uniaxial tension, with (a) non-auxetic micro-structural patterns and (b) auxetic micro-structural patterns (Bonfanti and Bhaskar, 2019). For conventional sheets, wrinkles develop at the center of the sheet. For auxetic sheets, they appear near the clamped edges. Bottom row: Buckling profiles (according to the magnitude of the displacement field) obtained with ABAQUS and the Blatz–Ko model Eq. (1). Here $\alpha = 0.4$, $\mu = 0.53$ GPa, and $\nu = 0.38, -0.2$ in (c) and (d), respectively. The sheet is modeled using 3D shell elements in ABAQUS, where the geometry lies in the global X–Z plane and the initial shell thickness is oriented along the Y-axis. Uniaxial stretch is applied along the X-direction, and wrinkling amplitudes occurs as out-of-plane displacement along Y-direction.

replicate the experimental observations of Choi and Lakes (1992) on auxetic structures. The Blatz–Ko strain energy function is as follows,

$$W = c_1\left(I_1 - 3 + \frac{1}{\beta}\left(I_3^{-\beta} - 1\right)\right) + c_2\left(\frac{I_2}{I_3} - 3 + \frac{1}{\beta}\left(I_3^{\beta} - 1\right)\right), \tag{1}$$

where $c_1 = \alpha\frac{\mu}{2}$, $c_2 = (1-\alpha)\frac{\mu}{2}$, $\beta = \frac{\nu}{1-2\nu}$, $\mathbf{F}$ is the deformation gradient, and $I_1 = \mathrm{tr}(\mathbf{F}\mathbf{F}^T)$, $I_2 = I_3\mathrm{tr}[(\mathbf{F}\mathbf{F}^T)^{-1}]$, $I_3 = \det(\mathbf{F}\mathbf{F}^T)$ are three strain invariants. Also, the material constants are the non-dimensional parameter $0 < \alpha < 1$, the initial shear modulus $\mu > 0$, and the Poisson ratio $-1 < \nu \leq 1/2$.

Fig. 2 shows that the Blatz–Ko model can effectively capture the experimentally observed behavior of thin membranes (without a substrate) under tension, encompassing both auxetic and conventional Poisson ratios. The model accurately distinguishes the differences in the wrinkling patterns between auxetic and conventional materials, aligning with the experimental findings of Bonfanti and Bhaskar (2019), who studied thin acetate sheets with laser-cut microstructural patterns.

Although wrinkling in bilayers (Fig. 1) and freestanding films (Fig. 2) represent two distinct classes of problems in terms of wrinkle morphology, onset, and location, Fig. 2 demonstrates that the Blatz–Ko model can predict wrinkling behavior in compressible systems, including those with auxetic characteristics.

To conduct the ABAQUS simulations of Fig. 2(c,d), we implemented the Blatz–Ko model using a user-defined hyperelastic subroutine (UHYPER), and then performed a linear buckling analysis to determine the onset of wrinkling. Here, instead of explicitly modeling the microstructural patterns, we assigned effective material properties representative of auxetic and conventional behavior to the films. This approach allows for a direct comparison between numerical predictions from homogenized models and experimental observations of microstructured models.

2.2. Semi-analytical treatment: linear buckling analysis

To establish a consistent notation for the bilayer system, we denote variables associated with the film and substrate layers using the letters f and s, respectively.

To determine the critical stretch and wavelength of the wrinkling instability, we employ the small-on-large method: we first compute the base (elastic) solution, and then superimpose an incremental deformation and derive, and solve, the incremental governing equations and boundary conditions.

The Blatz–Ko model (1) is used to obtain the principal components of the Cauchy stress $\mathbf{T}$ as follows:

$$T_{ii} = \frac{E}{2(1+\nu)}J^{-(2\alpha+1)}\left[-\alpha + [(\alpha-1)\lambda_i^{-2} + \alpha\lambda_i^2]J^{2\alpha} - (\alpha-1)J^{4\alpha}\right], \qquad \text{(no summation over } i\text{)}, \tag{2}$$

where λ_i are the principal stretch ratios and $J = \det\mathbf{F}$.

For the substrate, which is subjected to uniaxial tension along the X–direction, the stress conditions impose $T_{22}^s = T_{33}^s = 0$, leading to the following deformation gradient:

$$\mathbf{F}^s = \mathrm{diag}\left[\lambda_1^s, (\lambda_1^s)^{-\nu_s}, (\lambda_1^s)^{-\nu_s}\right]. \tag{3}$$

Because the film and substrate are perfectly bonded, they experience the same stretches in the $X-$ and $Z-$directions, so that $\lambda_1^f = \lambda_1^s = \lambda_1$, $\lambda_3^f = \lambda_3^s = (\lambda_1^s)^{-\nu_s}$. Furthermore, the transverse stress component satisfies $T_{22}^f = T_{22}^s = 0$. Applying these conditions, we find the deformation gradient for the film as:

$$\mathbf{F}^f = \mathrm{diag}\left[\lambda_1, \lambda_1^{\widetilde{\nu}}, \lambda_1^{-\nu_s}\right], \qquad \widetilde{\nu} = \frac{\nu_f(\nu_s - 1)}{(1-\nu_f)}. \tag{4}$$

Because the two components are perfectly bonded and the system is treated as effectively infinite in-plane, spatial variations in the deformation gradient are neglected. This modeling approach aligns with the classical analyses of wrinkling in bilayer systems, such as thin-film coatings on semi-infinite substrates, where edge effects are absent and the pre-buckling deformation is assumed to be homogeneous (Cai and Fu, 1999; Cao and Hutchinson, 2012b; Alawiye et al., 2019).

Eqs. (3) to (4), together with the stress expression in Eq. (2), define the base state (elastic solution) of the bilayer under tension.

To determine the onset of wrinkling, a small-amplitude displacement $\mathbf{u}$ is superimposed on the finite deformations given in Eqs. (3) to (4). Following the incremental approach outlined by Haughton and Ogden (1978), the resulting incremental equilibrium equations are derived as follows:

$$\begin{aligned} &\mathcal{A}^s_{0jilm} u^s_{m,lj} = 0, && -\infty < y < 0, \\ &\mathcal{A}^f_{0jilm} u^f_{m,lj} = 0, && 0 < y < h, \end{aligned} \tag{5}$$

where the commas denote differentiation with respect to the current coordinates, h is the current thickness of the film, and $\mathcal{A}_0$ is the fourth-order tensor of the instantaneous elastic moduli, with components:

$$\mathcal{A}_{0jilm} = J^{-1} F_{j\alpha} \frac{\partial^2 W}{\partial F_{i\alpha} \partial F_{m\beta}} F_{l\beta}. \tag{6}$$

We look for solutions in the form:

$$u_z = e^{\gamma y} \sin(kz), \qquad u_y = e^{\gamma y} \cos(kz), \tag{7}$$

where γ is the attenuation coefficient and k is the wavenumber of the sinusoidal wrinkles. Substitution into Eq. (5) leads to an eigenproblem, with characteristic equation a bicubic in γ. In the film, the general solution is of the form:

$$u_z^f = \left(\sum_{i=1}^{4} \mathcal{V}_i e^{\gamma_i y}\right) \sin(kz), \quad u_y^f = \left(\sum_{i=1}^{4} \mathcal{V}_i e^{\gamma_i y}\right) \cos(kz), \tag{8}$$

where $\gamma_1, \ldots, \gamma_4$ are the eigenvalues, and $\mathcal{V}_1, \ldots, \mathcal{V}_4$ are constants.

In the substrate, the stretch ratios along the $Y-$ and $Z-$ directions are equal, and $\gamma = 1$ is a repeated eigenvalue. The other repeated root, $\gamma = -1$ is discarded to enforce decay. Therefore, the solution is of the form:

$$u_z^s = (\mathcal{U}_1 + \mathcal{U}_2 y) e^y \sin(kz), \qquad u_y^s = (\mathcal{U}_1 + \mathcal{U}_2 y) e^y \cos(kz), \tag{9}$$

where $\mathcal{U}_1, \mathcal{U}_2$ are constants.

By applying the traction-free boundary conditions:

$$\mathcal{A}^f_{02ilm} u^f_{m,l} = 0, \qquad y = h, \tag{10a}$$

and the continuity conditions:

$$\mathcal{A}^f_{02ilm} u^f_{m,l} = \mathcal{A}^s_{02ilm} u^s_{m,l}, \qquad u_i^f = u_i^s, \qquad y = 0, \tag{10b}$$

we obtain six homogeneous equations for $\{\mathcal{U}_1, \mathcal{U}_2, \mathcal{V}_1, \ldots, \mathcal{V}_4\}$. The bifurcation condition is then given by equating the determinant of a 6×6 coefficient matrix to 0. This condition provides the foundation for the following asymptotic analysis.

2.3. Asymptotic analysis

Prior studies have predominantly examined the wrinkling of elastic bilayers subjected to uniaxial tension in the context of linear elasticity. To derive expressions for the critical strain ε_c and critical wavenumber k_c (Biot, 1937; Timoshenko et al., 1959), a two-step approach was adopted.

First, the critical compressive strain for a linear elastic bilayer system is derived by imposing the plane-strain condition. This derivation follows the classical ordinary differential equation governing the bending of a thin elastic beam, modeled under plane-stress conditions, on a semi-infinite elastic foundation subjected to a compressive load (Allen, 1969b; Cai and Fu, 2000). Second, the difference in lateral contraction between the substrate and film layers is used to approximate the critical strain under applied tensile loading.

This approach resulted in the following expressions, derived by Volynskii et al. (2000), Chung et al. (2011), and Nikravesh et al. (2019a):

$$\varepsilon_c = \frac{1}{4(\nu_s - \nu_f)} \left(3 \frac{\mu_s}{\mu_f} \frac{1-\nu_f}{1-\nu_s}\right)^{2/3}, \qquad k_c h = \left(3 \frac{\mu_s}{\mu_f} \frac{1-\nu_f}{1-\nu_s}\right)^{1/3}, \tag{11}$$

for linearly elastic bilayers under uniaxial tension. These expressions are used in buckling-based metrology applications to calculate the Young modulus of the film, but they are only valid for low strains ($\ll 10\%$) and under the assumption of plane strain Stafford et al. (2004).

However, it is important to note that the plane-strain assumption used in the derivation of Eq. (11) is not valid for a bilayer system under uniaxial tension. To address this gap, we follow Cai and Fu (2000, 2019) and assume that the shear modulus ratio $r = \mu_s/\mu_f$ is of the order $(k_c h)^3$ to derive asymptotic expressions for the critical strain and wavenumber. For simplicity, we set $\alpha_s = \alpha_f = 1$ in Eq. (1) and focus on the compressible neo-Hookean strain energy function for both the film and substrate layers:

$$W^{\mathrm{nH}} = \frac{\mu}{2}\left[I_1 - 3 + \frac{1-2\nu}{\nu}\left(I_3^{-\frac{\nu}{1-2\nu}} - 1\right)\right]. \tag{12}$$

To derive the asymptotic expressions for the critical strain and wavenumber, we introduce the following ansatz:

$$k_c h = \sum_{i=1}^{5} d_i \delta^i + \mathcal{O}(\delta^6), \quad \lambda_c = 1 + \sum_{\substack{i=1 \\ i\neq 2}}^{6} c_i \delta^i + \mathcal{O}(\delta^7), \quad \delta = \left(\frac{\mu_s}{\mu_f}\right)^{1/3} = r^{1/3}. \tag{13}$$

From Eq. (4), the component F_{22}^f can be expanded as a series in terms of δ, as:

$$F_{22}^f = \lambda_1^{\tilde{\nu}} = 1 + \sum_{i=1}^{8} \hat{d}_i \delta^i + \mathcal{O}(\delta^9). \tag{14}$$

Similarly, the attenuation coefficients for the film layer $\gamma_1, \ldots, \gamma_4$ and their squares can be expressed as series expansions in terms of δ up to eight terms. These approximations significantly reduce computational complexity.

Next, we substitute the expressions for the attenuation coefficients $(\gamma_1, \ldots, \gamma_4)$, $k_c h$, λ_c, and F_{22}^f into the bifurcation equation and its derivative with respect to $k_c h$, then expand both in terms of δ. These expansions are truncated to 12 and 11 terms, respectively, with higher-order terms omitted for simplicity.

Finally, to determine the unknown parameters, we impose the condition that the coefficients of δ^i and δ^{i-1} in the bifurcation equation and its derivative (for all $i \geq 8$) vanish simultaneously. This yields recursive relations for c_{j+1} and d_j for $j \geq 1$.

Using this procedure, we obtain the asymptotic expressions for the critical stretch and wavenumber:

$$\begin{aligned}
\lambda_c &= 1 + \frac{\left[(1-\nu_f)(1-\nu_s)\right]^{2/3}}{(\nu_s - \nu_f)\left(8\nu_s/3 - 2\right)^{2/3}} r^{2/3} + \frac{(1-\nu_f)(2\nu_s - 1)}{(\nu_s - \nu_f)(4\nu_s - 3)} r + c_4 r^{4/3} + c_5 r^{5/3} + c_6 r^2 + \mathcal{O}(r^{7/3}), \\
k_c h &= \left[\frac{4(1-\nu_f)(1-\nu_s)}{1 - 4\nu_s/3}\right]^{1/3} r^{1/3} + d_3 r + d_4 r^{4/3} + d_5 r^{5/3} + \mathcal{O}(r^2),
\end{aligned} \tag{15}$$

where the coefficients $c_4, \ldots, c_6, d_3, \ldots, d_5$ are provided in Appendix B.

The asymptotic expressions in Eq. (15) will be employed to compute the critical stretch ratio and critical wavenumbers for compressible neo-Hookean bilayer systems, as discussed in Section 3.4.

2.4. Homogenization and inverse analysis

Within a small-strain framework, the homogenized elastic stiffness $\overline{\mathbb{C}}$ is defined as

$$\overline{\mathbb{C}} = \frac{\partial \overline{\boldsymbol{T}}}{\partial \overline{\boldsymbol{\varepsilon}}}, \tag{16}$$

where $\overline{\boldsymbol{T}}$ and $\overline{\boldsymbol{\varepsilon}}$ denote the homogenized Cauchy stress and homogenized small-strain tensors, respectively. These quantities are obtained by averaging the local stress $\boldsymbol{T}$ and strain $\boldsymbol{\varepsilon}$ over the volume of the unit cell Ω:

$$\overline{\boldsymbol{T}} = \frac{1}{\Omega}\int_{\Omega} \boldsymbol{T}\, \mathrm{d}\Omega, \qquad \overline{\boldsymbol{\varepsilon}} = \frac{1}{\Omega}\int_{\Omega} \boldsymbol{\varepsilon}\, \mathrm{d}\Omega. \tag{17}$$

The homogenized stiffness in Eq. (16) can be computed using various approaches, such as FE-based periodic homogenization (Hassani and Hinton, 1998) or FFT-based techniques (Moulinec and Suquet, 1998). However, in inverse analysis, the iterative nature of the inverse design procedure makes it impractical to directly use these homogenization schemes. An alternative approach is to construct machine learning surrogate models using datasets generated from the aforementioned physics-based methods, thereby enabling the inverse design process.

Danesh et al. (2024) adopted this latter approach for the inverse design of auxetic unit cells, where, first, the forward surrogate models $\mathcal{S}$ are generated to predict the homogenized elastic stiffness constants $\overline{C}_{ijkl} = \mathcal{S}(\mathbf{g}, \mathbf{m})$ as functions of the vectors $\mathbf{g}$ and $\mathbf{m}$, denoting the geometric and material input parameters, respectively. Then, the inverse problem is solved to obtain the unit cell's geometric parameters by minimizing the loss between the target homogenized stiffness component $\hat{\overline{C}}_{ijkl}$ and its counterpart predicted by the surrogate model $\overline{C}_{ijkl}$. The loss function is defined as a weighted sum of squared differences between the predicted and target homogenized stiffness components:

$$\mathcal{L}_{\mathrm{inv}} = \frac{1}{n_c}\sum_{m=1}^{n_{\mathrm{ind}}} w_m \left(\overline{C}_{ijkl} - \hat{\overline{C}}_{ijkl}\right)^2. \tag{18}$$

The index m enumerates the n_{ind} independent components of the stiffness tensor $\overline{\mathbb{C}}$. Each independent component $\overline{C}_{ijkl}$ corresponds to a specific m, and the Boolean variable w_m determines whether that particular component is included in the loss calculation ($w_m = 1$) or ignored ($w_m = 0$). The normalization factor $n_c = \sum_{m=1}^{n_{\text{ind}}} w_m$ ensures that the loss is averaged over only the selected components. Although the summation is formally written over m, it implicitly accounts for all relevant C_{ijkl} components through their indexing. For orthogonal void auxetic unit cells, the presence of symmetry axes results in orthotropic stiffness characterized by three independent elastic constants (i.e. $n_{\text{ind}} = 3$).

Minimizing the loss function in Eq. (18) using gradient-based optimization (Zheng et al., 2021) or grid search algorithms (Danesh et al., 2024) yields the optimal geometric parameters that achieve the desired homogenized stiffness. We use this approach in Section 3.5 to determine the geometric parameters of auxetic unit cells with the desired Poisson ratios.

3. Finite element simulations: 3D models

This section presents our FE approach using 3D models to study wrinkling in homogenized bilayers and those with microstructured films of different material properties. Initially, we establish and validate our numerical setup. We then explore two case studies: one that examines bilayers with nearly incompressible substrates and the other with highly auxetic films. Our analysis concludes with predictions from asymptotic expressions and the application of inverse analysis techniques, followed by a comparison of the buckling behavior of bilayers with microstructured films with predictions from homogenized models.

3.1. Numerical setup and validation

To validate the accuracy of our implementation of periodic boundary conditions (PBCs) using a Python script, we conducted a preliminary study using a linear buckling analysis for an incompressible neo-Hookean bilayer under 2D (plane-strain) compression. The bilayer was periodic along the $X-$direction (see Appendix A), and we successfully recovered the results reported by Cao and Hutchinson (2012b), confirming the reliability of our approach.

Following this validation, we performed a series of FE simulations to investigate wrinkling in 3D bilayers subjected to uniaxial tension. The bilayers were modeled using the Blatz–Ko strain energy function, considering two primary configurations: one with a nearly incompressible substrate and the other with a highly auxetic film.

The depth of the bilayer (in the $Z-$direction) was set as an integer multiple of the predicted wrinkling wavelength, calculated using semi-analytical results from Mathematica, for the cases: $(\nu_f, \nu_s) = \{0.3, 0.495\}$ and $\{-0.95, -0.8\}$. For other pairs of Poisson ratios, small variations in depth were observed to have a negligible effect on the critical stretch values, with changes only in the third decimal place.

To optimize computational efficiency without compromising accuracy, we used the following dimensions. For the nearly incompressible substrate case, the bilayer structure had dimensions (X, Y, Z) of $15 \times 45 \times 5.684$ units, with a thickness ratio of $h_s/h_f = 299$ (Section 3.2). In the case of the highly auxetic film, the dimensions were $15 \times 80 \times 4.504$ units, with a thickness ratio of $h_s/h_f = 399$ (Section 3.3). For the neo-Hookean bilayers ($\alpha_f = \alpha_s = 1$), the dimensions were $6 \times 45 \times 1.85$ units, with a thickness ratio of $h_s/h_f = 299$ (Section 3.4).

PBCs were applied on the extreme faces in the $X-$ and $Z-$directions of the domain using a user-defined Python script. Both the film and the substrate layers were modeled using a UHYPER subroutine with the Blatz–Ko strain energy function. FE discretization was performed using 20-node hexahedral elements with quadratic interpolation and reduced integration (C3D20R) for both the film and substrate layers. For the limiting case of incompressibility, C3D20RH elements were used. For the Blatz–Ko bilayers, the FE mesh consisted of 34,200 elements for the nearly incompressible substrate case (Section 3.2) and 17,130 elements for the highly auxetic film case (Section 3.3).

Cai and Fu (1999) demonstrated that the stability of a coated elastic half-space depends on the shear modulus ratio $r = \mu_s/\mu_f$. The system is less stable than half-space when $r < 1$ and more stable when $r > 1$. In the former case, there exists a critical wavenumber corresponding to a minimum critical compression. Physically, when the film is stiffer than the substrate ($r < 1$), it carries the majority of the load, resulting in the buckling of the film layer as an energetically favorable state. This occurs because the system minimizes its total energy by allowing the film to buckle rather than undergo uniform compression. In contrast, when the film is softer than the substrate ($r > 1$), the stability of the half-space increases, suppressing wrinkling and favoring homogeneous in-plane deformation.

For neo-Hookean bilayers, Cao and Hutchinson (2012b) observed that when the film is sufficiently stiff ($r < 0.1$), sinusoidal wrinkling remains the stable and preferred mode for relatively large compressions before the onset of period-doubling. However, when the film is relatively soft ($r > 0.5$), surface creases (nonlinear buckling) can emerge within the film before the bifurcation mode of wrinkling, as noted by Hong et al. (2009).

Based on these observations, we set the Blatz–Ko parameters to $\alpha_f = \alpha_s = 0.4$ and the shear modulus ratio to $\mu_f/\mu_s = 30$ or $r = 1/30$ in our FE simulations.

For 3D bilayer systems under large uniaxial tension, we found that wrinkles were observed only when the Poisson ratio of the film (ν_f) was lower than that of the substrate (ν_s). This result is consistent with the findings of Nikravesh et al. (2019a), which were obtained for linear-elastic bilayer systems.

It is also consistent with the observation that wrinkling is associated with the presence of compressive stress in the film, in the direction transversal to the applied tension, that is, along the $Z-$direction. To visualize this intuition, we illustrate two possible

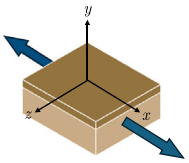

Undeformed bilayer

Poisson's ratios	$\nu_f \geq \nu_s$	$\nu_f < \nu_s$
Unconstrained virtual state	(a) 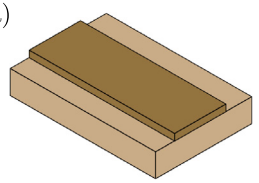	(b) 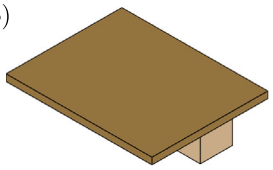
Final deformed state	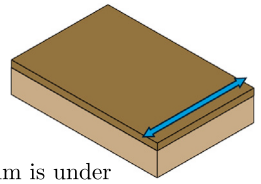 Film is under lateral **tension**	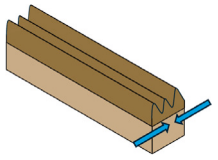 Film is under lateral **compression**
Wrinkles	No	**Yes**

Fig. 3. A bilayer under tension. (a) The film's Poisson ratio is larger than that of the substrate ($\nu_f \geq \nu_s$). If the two layers were free from any constraint, the film's width would be less than that of the substrate. However, due to bonding, in the final deformed state of the bilayer, the film is under lateral tension and no wrinkles may develop. (b) The film's Poisson ratio is smaller than that of the substrate ($\nu_f < \nu_s$). In an ideal unconstrained state, the film's width would be greater than that of the substrate. Thus, in the final deformed state, the film is under lateral compression and wrinkles may develop.

scenarios in Fig. 3. We introduce a virtual unconstrained configuration, which represents the state that each layer of the bilayer would adopt under tension if it were not bonded to the other.

In Scenario (a), the film has a larger Poisson ratio than the substrate. In their unconstrained states under tension, the film's lateral dimension would be less than that of the substrate. However, because the layers are bonded, the film is forced to expand laterally to match the substrate, resulting in tensile stresses perpendicular to the applied tension.

Conversely, Scenario (b) considers the opposite situation, when the film has a smaller Poisson ratio than the substrate. Then the film is forced to contract, leading to compressive stresses, and eventually, to wrinkles.

Following Fig. 3, we pick two cases along these two scenarios to study wrinkling in the layered system under uniaxial tension. We find that the numerical results obtained using different approaches in the software ABAQUS and Mathematica match well for a wide range of material parameters.

3.2. Nearly incompressible substrate

First, we assume that the substrate is nearly incompressible ($\nu_s = 0.495$), while the film's Poisson ratio varies within the range $\nu_f \in [-0.95, 0.495)$. When the substrate has a higher Poisson ratio than the film, it undergoes greater transverse compression ($Z-$direction) under uniaxial tension applied along the $X-$direction. This mismatch in deformation between the layers generates compressive stresses in the film, leading to wrinkle formation parallel to the $X-$direction (see Fig. 1).

Variations in the critical stretch for wrinkling λ_c and the corresponding critical wavenumber k_c are plotted against ν_f in Fig. 4(a–b). As shown in Fig. 4(a), the critical stretch values predicted by the semi-analytical analysis (Mathematica) and the FE buckling analysis (ABAQUS) align well for $\nu_f \leq 0.35$. However, beyond this threshold, ABAQUS ceases to predict wrinkles in the desired direction and instead returns negative eigenvalues. This suggests that the load direction must be reversed to obtain wrinkles, which is unphysical and indicates a breakdown of the numerical predictions.

For an auxetic film ($\nu_f < 0$), expansion occurs in all directions under tension, while the nearly incompressible substrate contracts along the $Z-$direction, generating compressive stress in the film. Consequently, wrinkles form at lower critical stretch values. As the Poisson ratio of the film approaches that of the substrate, the critical stretch required for wrinkling increases sharply.

3.3. Highly auxetic film

To examine the effect of a highly auxetic film, we consider a film layer with a negative Poisson ratio, $\nu_f = -0.95$, while varying the Poisson ratio of the substrate within the range $\nu_s \in (-0.95, 0.495]$.

Fig. 4(c–d) displays the variations in the critical stretch λ_c and the wavenumber k_c as a function of ν_s. Our numerical results from ABAQUS and semi-analytical predictions from Mathematica show strong agreement in the range $-0.7 \leq \nu_s \leq 0.495$. However, for $\nu_s < -0.8$, ABAQUS fails to provide meaningful predictions.

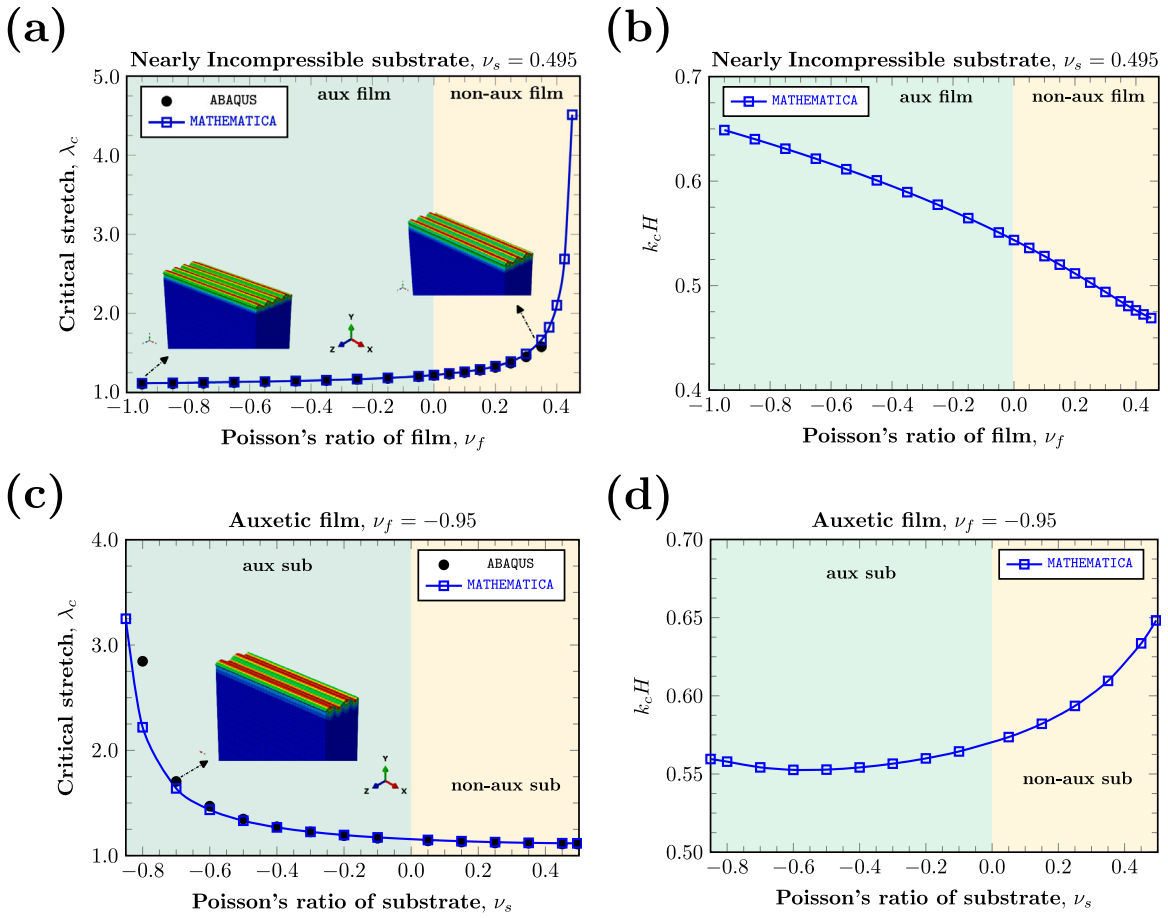

Fig. 4. Numerical simulations using Blatz–Ko material model (Eq. (1)). Variations of the critical stretch of wrinkling λ_c and corresponding critical wavenumber measure $k_c H$ with the Poisson ratio of one layer (k_c is the critical wavenumber and H is the film initial thickness). We set the shear modulus ratio to $\mu_f/\mu_s = 30$, i.e. $r = 1/30$. (a–b): The substrate is nearly incompressible ($\nu_s = 0.495$). (c–d): The film is highly auxetic ($\nu_f = -0.95$). Results from ABAQUS: black dots, results from Mathematica: solid line with square markers.

The results indicate that buckling generally occurs at lower stretch values for highly auxetic films. However, when ν_s approaches ν_f, the film and substrate exhibit similar levels of transverse contraction. As a result, the compressive stress developed in the film layer is insufficient to induce wrinkle formation.

Typically, the wavelength of wrinkles increases as the Poisson ratios of the film and substrate approach each other and decreases as they diverge, as shown in Fig. 4(b,d). However, when the film and substrate are highly compressible ($\nu_f = -0.95$ and $\nu_s \leq -0.7$), this trend reverses, and the wavelength decreases, as illustrated in Fig. 4(d).

Notably, this behavior is not observed in compressible neo-Hookean bilayers (Eq. (12)). This can be verified by plotting the asymptotic expression for the critical wavenumber (Eq. (15)), which remains a monotonically decreasing function as the Poisson's ratios of the film and substrate approach each other. The distinct behavior observed in Blatz–Ko-type materials for $\nu_s \leq -0.7$ deviates from expected trends and can be further explored in future work.

In summary, we found that to ensure early wrinkling in a bilayer subjected to uniaxial tension, a large contrast in the Poisson ratio between the film and the substrate is required. This effect is particularly pronounced when one material is auxetic and the other is non-auxetic, highlighting the critical role played by the Poisson ratio contrast in governing instabilities in bilayer systems.

3.4. Asymptotic solution: Compressible bilayer system

To further analyze the influence of material nonlinearity and Poisson ratio contrast, we compare the predictions from linear (Eq. (11)) and hyperelastic models (Eq. (15)).

When strains are small, the asymptotic expressions for compressible neo-Hookean bilayers (Eq. (12)) recover the predictions of the linear elastic model. However, as ν_f approaches ν_s, the critical strain increases significantly and the linear elastic model (Eq. (11)) fails to capture accurate behavior due to the breakdown of the plane-strain assumption and the effects of non-linearities

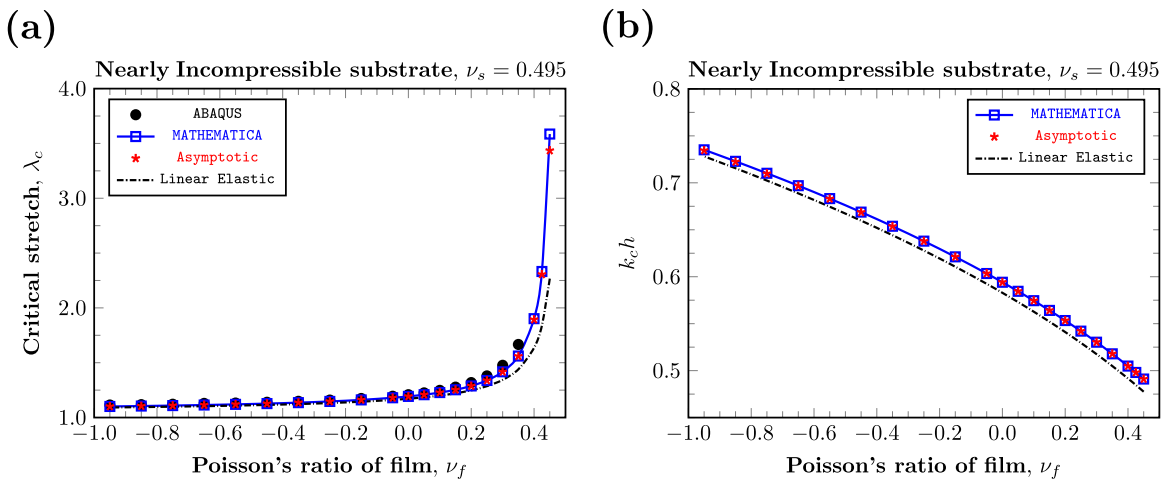

Fig. 5. Numerical simulations for a bilayer made of compressible neo-Hookean materials ($\alpha_s = \alpha_f = 1$ in Eq. (1)). The substrate is nearly incompressible ($\nu_s = 0.495$). We set the shear modulus ratio to $\mu_f/\mu_s = 30$, i.e. $r = 1/30$. (a–b): Variations of the critical stretch of wrinkling λ_c and corresponding critical wavenumber measure $k_c h$ (k_c: critical wavenumber, h: current film thickness) with the Poisson ratio of film layer ν_f. ABAQUS: black dots, Mathematica: solid line with square markers, Asymptotic expressions (Eq. (15)): star markers, Linear-elastic expressions (Eq. (11)): dash-dotted line.

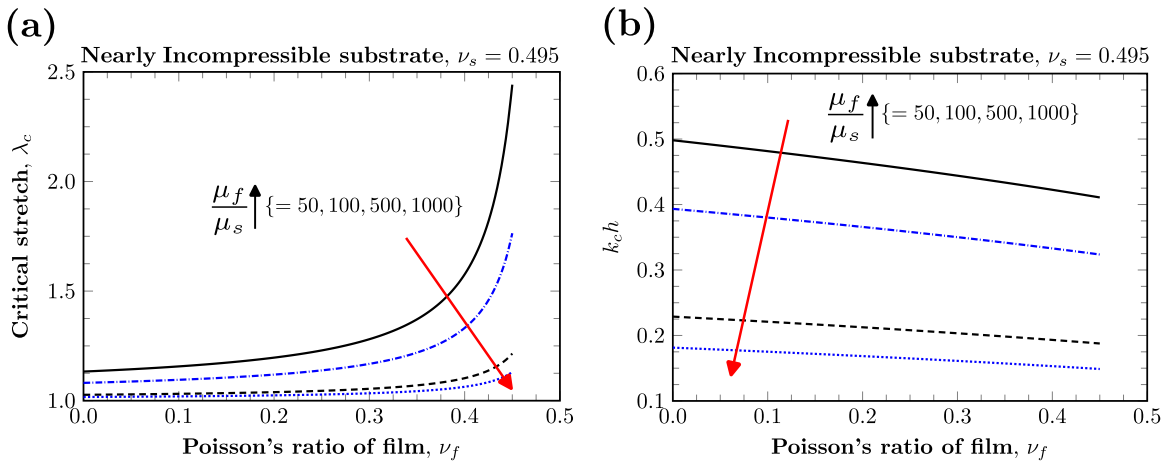

Fig. 6. Using the asymptotic expressions Eq. (15) for compressible neo-Hookean materials ($\alpha_s = \alpha_f = 1$ in Eq. (1)). The substrate is nearly incompressible ($\nu_s = 0.495$). (a–b): Variations of the critical stretch of wrinkling λ_c and corresponding critical wavenumber measure $k_c h$ with the Poisson ratio of film layer (k_c is the critical wavenumber and h is the deformed film thickness) and for contrast in shear moduli between the layers ($\mu_f/\mu_s = \{50, 100, 500, 1000\}$).

in geometric and material parameters. Consequently, linear elastic expressions substantially underestimate numerical results from ABAQUS and Mathematica, whereas the hyperelastic model remains in good agreement.

When the film layer is highly auxetic ($\nu_f \to -0.95$), the plane-strain condition remains approximately valid as $\lambda_c \to 1$. In this regime, the linear elastic model aligns well with numerical results and the asymptotic solution. This behavior is illustrated in Fig. 5(a), which shows the variation of λ_c with ν_f for a nearly incompressible substrate ($\nu_s = 0.495$).

In Fig. 5(b), although a similar trend is observed in both linear and nonlinear models, we see that the linear elastic model consistently underpredicts the critical wavenumber compared to numerical and asymptotic results. In particular, when the Poisson ratio contrast is high (low), wrinkles exhibit shorter (longer) wavelengths, as seen in Fig. 4.

Fig. 6 illustrates the dependence of λ_c and $k_c h$ on ν_f for different shear modulus contrasts μ_f/μ_s. According to Eq. (15), with r assumed to be on the order of $(k_c h)^3$, an increase in μ_f/μ_s or a decrease in r results in a lower critical stretch and wavenumber, leading to early buckling and long-wavelength wrinkles.

For compressible neo-Hookean bilayers, the critical stretch ratio for buckling and the wrinkle wavelength increase as the Poisson ratios of the film and substrate approach each other. Asymptotic expressions generate curves instantly, offering a computationally efficient alternative to the ABAQUS simulations. Building on these findings, we extend our analysis to homogenization and inverse techniques, with the aim of tailoring auxetic microstructures to achieve desired material properties.

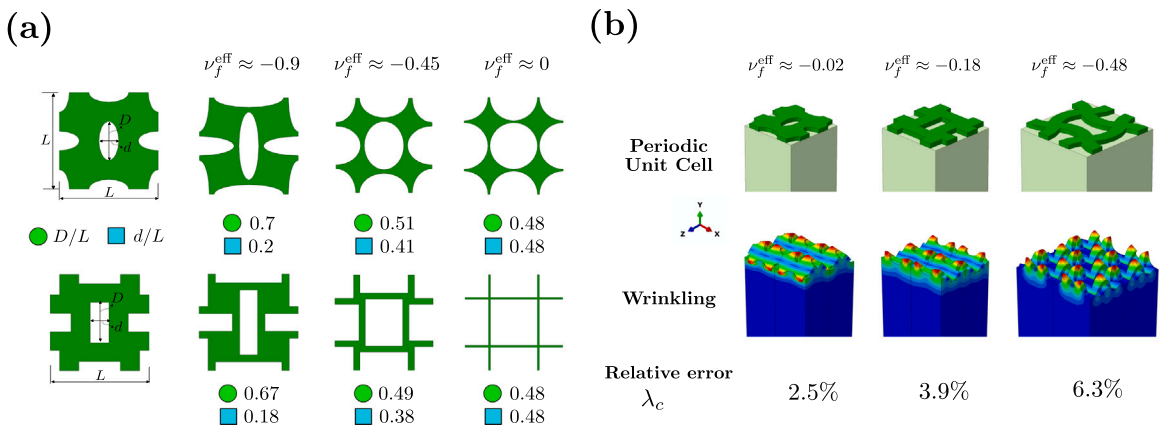

Fig. 7. (a) Influence of microstructural geometry on the effective Poisson ratio (ν_f^{eff}) in auxetic films with orthogonal-oval and rectangular-void patterns. Films with desired effective Poisson's ratios are obtained using inverse analysis. (b) Comparison of undeformed and deformed configurations in bilayers with distinct auxetic microstructures, each designed to achieve specific Poisson's ratios in the small-strain regime. Film and substrate base materials exhibit compressible ($\nu_f = 0.1$) and nearly incompressible ($\nu_f = 0.495$) properties, respectively. Periodic boundary conditions are applied on the lateral faces of the domain along X and Z and the system is subjected to uniaxial tension along X. We observe that the wrinkles are generated parallel to the direction of tension. The bottom of (b) shows the percentage relative error in critical stretch between homogenized bilayers (Fig. 4(a)) and those with microstructural patterns, obtained in ABAQUS with the Blatz–Ko model.

3.5. Inverse design and homogenization: Application

Based on the surrogate models developed by Danesh et al. (2024) for orthogonal void auxetic structures in the small-strain regime, we use an inverse design approach to efficiently determine the geometric parameters of a chosen auxetic unit cell. This method precisely tailors the unit cell to achieve specific components of effective elastic stiffness based on the material properties of the base constituent. Using the Voigt notation, Danesh et al. (2024) reported that, due to the inherent orthogonal symmetry of these auxetic unit cells with orthogonal voids, the effective stiffness tensor simplifies to an orthotropic form characterized by only three distinct elastic constants: $\overline{C}_{11}(=\overline{C}_{22})$, $\overline{C}_{12}(=\overline{C}_{21})$, and $\overline{C}_{33}$. This symmetry leads to the following linear relationship between the in-plane effective stress and strain:

$$\begin{pmatrix} \overline{T}_{11} \\ \overline{T}_{22} \\ \overline{T}_{12} \end{pmatrix} = \begin{pmatrix} \overline{C}_{11} & \overline{C}_{12} & 0 \\ \overline{C}_{12} & \overline{C}_{11} & 0 \\ 0 & 0 & \overline{C}_{33} \end{pmatrix} \begin{pmatrix} \overline{\varepsilon}_{11} \\ \overline{\varepsilon}_{22} \\ 2\overline{\varepsilon}_{12} \end{pmatrix}. \tag{19}$$

Here, the notation $\overline{(\bullet)}$ refers to the homogenized average value of a quantity, including stress, strain, and elastic stiffness components, as described in Section 2.4. Therefore, if we define the components of the effective stiffness $\overline{C}_{11}$ and $\overline{C}_{12}$, we can obtain the desired effective Poisson's ratio $\nu_f^{\text{eff}} = \overline{C}_{12}/\overline{C}_{11}$.

We now demonstrate how our analysis can be used to predict wrinkling instabilities in bilayers with auxetic patterns. In fact, auxetic properties can be obtained at a continuum level with a careful design of holes or voids at the microscale (Lakes, 1993; Bertoldi et al., 2017).

Fig. 7(a) illustrates how the geometric parameters of orthogonal-oval and rectangular voids influence the effective Poisson ratio (ν_f^{eff}). Using the inverse design approach described by Danesh et al. (2024), we designed a set of auxetic structures with the desired effective Poisson ratios (ν_f^{eff}) in the small-strain regime.

To validate the effective properties of these structures generated from the inverse design, we used the FE code FEAP (Taylor, 2014). For this purpose, we discretized the unit cells with linear quadrilateral elements and performed homogenization to compute the effective elastic stiffness. Periodic boundary conditions were applied by enforcing symmetric nodes on opposing boundaries. After computing the effective elastic stiffness of each unit cell, we confirmed that the designed unit cells accurately recovered the target effective Poisson ratios with high precision.

After understanding the effect of geometric parameters of voids on the effective Poisson ratio, we consider an isotropic material with base properties of Young's modulus $E_f = 110$ GPa and Poisson's ratio $\nu_f = 0.1$. Using the inverse design approach, we generated auxetic structures with targeted effective Poisson's ratios. Specifically, we designed film layers with orthogonal-oval, rectangular, and sinusoidal voids to achieve $\nu_f^{\text{eff}} = -0.02, -0.18$, and -0.48, respectively, in the small-strain regime. These structures were then used to analyze wrinkling behavior, as shown in Fig. 7(b).

Linear perturbation procedure is carried out using the BUCKLE function in ABAQUS to evaluate the critical stretch ratio corresponding to the onset of instability in bilayers with embedded microstructural patterns (Cao and Hutchinson, 2012b). This procedure involves a linearized eigenvalue analysis based on the global stiffness matrix, identifying the loading condition at which instability occurs. The critical stretch ratios obtained from the eigenvalue analysis show close agreement with the predictions of the

homogenized model presented in Fig. 4(a), with a maximum relative error of 6.3%. This agreement demonstrates the accuracy of our numerical method in predicting wrinkling instabilities in bilayers with engineered microstructures.

However, it is important to note that the ratio between the wrinkling wavelength and the characteristic size of the unit cell plays a crucial role in determining the validity of the homogenization approach. When the wrinkling wavelength is much larger than the microstructural length scale, classical homogenization yields accurate predictions because of clear scale separation. In Fig. 7(b), this scale separation is reduced for the sinusoidal void configuration, and two wrinkles are observed within a single unit cell, leading to a wavelength-to-unit-cell ratio of approximately 0.5. This limited separation results in increased discrepancies between the homogenized predictions and the full microstructural simulations. In contrast, for the oval and rectangular void configurations, a single wrinkle spans the entire unit cell, corresponding to a wavelength-to-unit-cell ratio of 1. In these cases, the homogenized model provides predictions with comparatively lower error.

Although the observed errors remain within a reasonable range, the results underscore a key limitation of classical first-order homogenization in regimes with weak scale separation. To address this limitation, higher-order homogenization techniques (Guo et al., 2025) or nonlocal continuum models (Maraghechi et al., 2024) are more appropriate when the wrinkling wavelength is smaller than the unit cell size.

4. Conclusions

Our study explores the possibility of harnessing wrinkles parallel to the direction of applied tension in 3D isotropic compressible bilayers subject to finite deformations. Particular emphasis was placed on configurations where the substrate is nearly incompressible and when the film is highly auxetic.

We adopted a semi-analytical approach using Mathematica to predict the onset of wrinkling. For the finite element aspect of our study, we developed a new UHYPER subroutine tailored for Blatz-Ko material models, along with custom Python scripts designed to simulate wrinkling in compressible bilayers under periodic boundary conditions. These scripts facilitate linear buckling analysis in FE simulations with ABAQUS.

For compressible neo–Hookean bilayer systems, we derived asymptotic expressions for the critical stretch ratio and critical wavenumber, which can be used under finite strains to determine the Young modulus of the film layer for buckling-based metrology applications.

We found that wrinkles can be obtained only when the Poisson ratio of the substrate is greater than that of the film. As the Poisson ratios of the film and substrate converge to a common value, the critical stretch ratio for buckling increase rapidly along with the wavelength of wrinkles. In the limiting case where the Poisson ratios of the film and substrate are equal, no wrinkling occurs, as the mismatch in in-plane deformation between the layers is not sufficient to generate the compressive stresses in the film required to trigger instability. Through multiple simulations, we showed that we can harness or delay the onset of wrinkles by varying the material properties.

Furthermore, using inverse analysis, we designed film microstructures to achieve desired effective Poisson ratios, validated with the FE code FEAP. The critical stretch ratio for buckling in auxetic structures with microstructural patterns aligns closely with predictions from homogenized models.

Some of the limitations of our work include the consideration of isotropic strain energy functions for auxetic structures and deformation-independent effective material properties.

Functional-grading of auxetics could also be explored with the methods presented in this study, see some preliminary works on harnessing instabilities in functionally-graded auxetic materials using tension-field theory (Venkata et al., 2023; Pamulaparthi Venkata et al., 2024) and their applications (Zhao et al., 2018; Zahoor et al., 2020; Babič et al., 2021).

Ultimately, the method developed in this work could play a critical role in the manufacturing and testing of auxetic hydrogel organ patches (Chansoria et al., 2022) and skin grafts (Gupta and Chanda, 2023). This approach could specifically guide the design of graft microstructures to prevent undesired wrinkling.

CRediT authorship contribution statement

Sairam Pamulaparthi Venkata: Writing – review & editing, Writing – original draft, Software, Formal analysis. **Yuxin Fu:** Writing – review & editing, Formal analysis. **Yibin Fu:** Writing – review & editing, Formal analysis. **Hooman Danesh:** Writing – review & editing, Software. **Michel Destrade:** Writing – review & editing, Methodology, Conceptualization. **Valentina Balbi:** Writing – review & editing, Methodology, Conceptualization.

Declaration of Generative AI and AI-assisted technologies in the writing process

During the preparation of this work, the authors used the ChatGPT-4o model to correct grammatical mistakes in the original text and to ensure that the paragraph structure was clear and cohesive. After using this tool, the authors reviewed and edited the content as needed and take full responsibility for the content of the published article.

Declaration of competing interest

The authors declare that they have no known competing financial interests or personal relationships that could have appeared to influence the work reported in this paper.

Acknowledgments

This project has received funding from the European Union's Horizon 2020 research and innovation programme under the Marie Skłodowska-Curie Grant Agreement No. 956401.

Appendix A. Validation of pbcs code – 2d incompressible neo-hookean bilayer model

Under uniaxial, plane-strain compression, the theoretical critical strain is $\varepsilon_c = {}^1\!/_4 \left(3\mu_s/\mu_f\right)^{2/3}$ (Cao and Hutchinson, 2012b).

In Fig. A.1, we applied PBCs on the left and right edges of the domain, roller support on the bottom edge of the substrate, perfect bonding between film and substrate layers, and traction-free condition on the top surface of the film in the two cases $\mu_f/\mu_s = 30, 1000$. We find $\varepsilon_c = 0.053, 0.0052$, respectively, matching well with the theoretical solutions.

Having validated our 1D PBCs script along the $X-$direction on a 2D model, we then extended the PBCs to two dimensions, along the $X-$ and $Z-$directions, to perform a linear buckling analysis on 3D bilayer systems under uniaxial tension.

The height ratio of substrate to film layers was taken as $h_s/h_f = 163$, with the width of layers being 30.457 units. We modeled both film and substrate with the incompressible neo-Hookean model.

We used a hybrid 8-node plane strain quadrilateral element with quadratic interpolation and reduced integration (CPE8RH) for both film and substrate layers. We also applied periodic boundary conditions on the left and right edges of the domain. The minimum size of the mesh element is lower than the height of the film. We took 12,800 elements, and the numerical results converged and were consistent with the theoretical solutions.

Appendix B. Coefficients in asymptotic expressions

The coefficients of the higher-order terms in Eq. (15) are given below:

$$c_4 = \frac{\mathcal{C}\left(45 + \nu_s c_{4a} + \nu_f c_{4b} + \nu_f^2 c_{4c}\right)}{20 \times 2^{1/3} \times 3^{2/3}(\nu_f - \nu_s)^2(-1+\nu_s)(-3+4\nu_s)^{4/3}}, \qquad c_5 = \frac{\mathcal{C}^2(-1+\nu_f)(-1+2\nu_s)(-3-4\nu_f+4\nu_s)}{2^{2/3} \times 3^{1/3}(\nu_f-\nu_s)^2(-3+4\nu_s)^{5/3}},$$
$$c_6 = \frac{4725 - 2\nu_f^4 c_{6a} - \nu_s c_{6b} + \nu_f^3 c_{6c} + \nu_f^2 c_{6d} + 2\nu_f c_{6e}}{12600(3-4\nu_s)^2(-1+\nu_s)^2(-\nu_f+\nu_s)^3}, \qquad \mathcal{C} = \left((1-\nu_f)(\nu_s-1)\right)^{1/3}, \tag{B.1a}$$

and

$$\begin{aligned}
c_{4a} &= -64 + (13-4\nu_s)\nu_s, \qquad c_{4b} = -71 + \nu_s(66 + (51-26\nu_s)\nu_s), \qquad c_{4c} = 56 - 92\nu_s + 26\nu_s^2,\\
c_{6a} &= 33727 + 2\nu_s(-73474 + \nu_s(122601 + \nu_s(-92584 + 26681\nu_s))),\\
c_{6b} &= 4410 + \nu_s(82574 + \nu_s(-288226 + \nu_s(399999 - 260716\nu_s + 67034\nu_s^2))),\\
c_{6c} &= 95848 + 2\nu_s(-138872 + \nu_s(46253 + \nu_s(235988 + \nu_s(-297317 + 106724\nu_s)))),\\
c_{6d} &= -3509 + \nu_s(-202720 + \nu_s(841376 + \nu_s(-1218634 + \nu_s(643241 + 2(22435 - 53362\nu_s)\nu_s)))),\\
c_{6e} &= -11970 + \nu_s(78479 + \nu_s(-137927 + \nu_s(-12652 + \nu_s(271583 + \nu_s(-276527 + 89714\nu_s))))).
\end{aligned} \tag{B.1b}$$

Similarly, the coefficients of higher-order terms in the asymptotic expression for critical wavenumber (Eq. (15)) are

$$d_3 = \frac{4 + 2\nu_s - 11\nu_s^2 + \nu_f\left(11 - 32\nu_s + 26\nu_s^2\right)}{15\left(3 - 7\nu_s + 4\nu_s^2\right)}, \qquad d_4 = \frac{\left(\frac{2}{3}\right)^{2/3}\mathcal{C}(1+2\nu_f)(-1+2\nu_s)}{(-3+4\nu_s)^{4/3}},$$
$$d_5 = \frac{\mathcal{C}^2\left(-6761 + \nu_s d_{5a} + 4\nu_f^2 d_{5b} - 2\nu_f d_{5c}\right)}{3150 \times 2^{2/3} \times 3^{1/3}(-1+\nu_f)(-1+\nu_s)^3(-3+4\nu_s)^{5/3}}, \tag{B.2a}$$

and

$$\begin{aligned}
d_{5a} &= 21724 + \nu_s(-19146 + \nu_s(-2636 + 7519\nu_s)), \qquad d_{5b} = 646 + \nu_s(-4964 + \nu_s(12906 + \nu_s(-14204 + 5791\nu_s))),\\
d_{5c} &= -3821 + \nu_s(7864 + \nu_s(5844 + \nu_s(-22796 + 13609\nu_s))).
\end{aligned} \tag{B.2b}$$

Data availability

No data was used for the research described in the article.

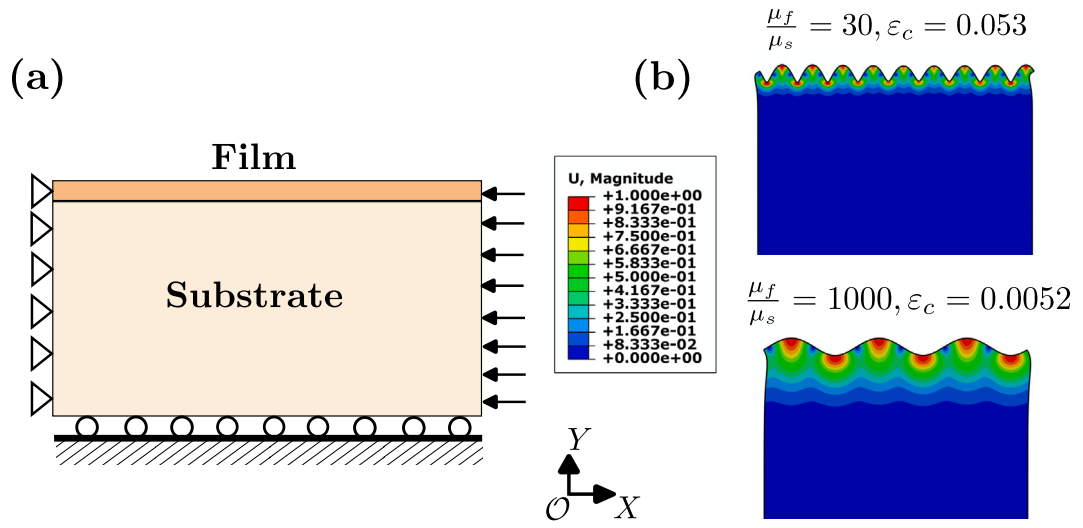

Fig. A.1. (a) Schematic representation of an incompressible neo-Hookean stiff film/soft substrate bilayer system under uniaxial compression. On the left edge of the domain, displacement and shear traction are set at zero. On the bottom edge of the domain, roller support restricts vertical displacement and shear traction, and the top surface of the film is traction-free. (b) Linear buckling solutions with critical strains ε_c when $\mu_f/\mu_s = 30, 1000$, in line with the predictions of Cao and Hutchinson (2012b).

References

ABAQUS Inc., 2019. ABAQUS/Standard User's Manual, Version 2019. Dassault Systèmes Simulia Corp, United States.

Alawiye, H., Kuhl, E., Goriely, A., 2019. Revisiting the wrinkling of elastic bilayers I: linear analysis. Phil. Trans. R. Soc. A 377 (2144), 20180076. http://dx.doi.org/10.1098/rsta.2018.0076.

Allen, H., 1969a. Analysis and design of structural sandwich panels.

Allen, H., 1969b. Chapter 8: Wrinkling and other forms of local instability. Anal. Des. Sandw. Panels 156–189.

Andres, S., Steinmann, P., Budday, S., 2018. The origin of compression influences geometric instabilities in bilayers. Proc. R. Soc. A: Math. Phys. Eng. Sci. 474 (2217), 20180267. http://dx.doi.org/10.1098/rspa.2018.0267.

Auguste, A., Jin, L., Suo, Z., Hayward, R.C., 2014. The role of substrate pre-stretch in post-wrinkling bifurcations. Soft Matter 10, 6520–6529. http://dx.doi.org/10.1039/C4SM01038H.

Babič, J., Laffranchi, M., Tessari, F., Verstraten, T., Novak, D., Šarabon, N., Ugurlu, B., Peternel, L., Torricelli, D., Veneman, J.F., 2021. Challenges and solutions for application and wider adoption of wearable robots. Wearable Technol. 2, e14.

Bakiler, A.D., Javili, A., 2023. Understanding the role of interfacial mechanics on the wrinkling behavior of compressible bilayer structures under large plane deformations. Math. Mech. Solids 28 (3), 748–772. http://dx.doi.org/10.1177/10812865221094833.

Bertoldi, K., Vitelli, V., Christensen, J., Van Hecke, M., 2017. Flexible mechanical metamaterials. Nat. Rev. Mater. 2 (11), 1–11. http://dx.doi.org/10.1038/natrevmats.2017.66.

Bigoni, D., Bordignon, N., Piccolroaz, A., Stupkiewicz, S., 2018. Bifurcation of elastic solids with sliding interfaces. Proc. R. Soc. A: Math. Phys. Eng. Sci. 474 (2209), 20170681. http://dx.doi.org/10.1098/rspa.2017.0681.

Biot, M.A., 1937. Bending of an infinite beam on an elastic foundation. J. Appl. Phys. 155–164. http://dx.doi.org/10.1063/1.1712886.

Biot, M.A., 1963. Surface instability of rubber in compression. Flow Turbul. Combust. 12, 168–182, URL: https://api.semanticscholar.org/CorpusID:116432730.

Biot, M.A., Taylor, G.I., 1957. Folding instability of a layered viscoelastic medium under compression. Proc. R. Soc. Lond. Ser. A. Math. Phys. Sci. 242 (1231), 444–454. http://dx.doi.org/10.1098/rspa.1957.0187.

Blatz, P.J., Ko, W.L., 1962. Application of finite elastic theory to the deformation of rubbery materials. Trans. Soc. Rheol. 6 (1), 223–252. http://dx.doi.org/10.1122/1.548937.

Bonfanti, A., Bhaskar, A., 2019. Elastic stabilization of wrinkles in thin films by auxetic microstructure. Extrem. Mech. Lett. 33, 100556. http://dx.doi.org/10.1016/j.eml.2019.100556.

Bowden, N., Brittain, S., Evans, A.G., Hutchinson, J.W., Whitesides, G.M., 1998. Spontaneous formation of ordered structures in thin films of metals supported on an elastomeric polymer. Nature 393 (6681), 146–149. http://dx.doi.org/10.1038/30193.

Brau, F., Damman, P., Diamant, H., Witten, T.A., 2013. Wrinkle to fold transition: influence of the substrate response. Soft Matter 9, 8177–8186. http://dx.doi.org/10.1039/C3SM50655J.

Cai, Z., Fu, Y., 1999. On the imperfection sensitivity of a coated elastic half-space. Proc. R. Soc. Lond. Ser. A Math. Phys. Eng. Sci. 455 (1989), 3285–3309. http://dx.doi.org/10.1098/rspa.1999.0451.

Cai, Z., Fu, Y., 2000. Exact and asymptotic stability analyses of a coated elastic half-space. Int. J. Solids Struct. 37 (22), 3101–3119. http://dx.doi.org/10.1016/S0020-7683(99)00071-2.

Cai, Z., Fu, Y., 2019. Effects of pre-stretch, compressibility and material constitution on the period-doubling secondary bifurcation of a film/substrate bilayer. Int. J. Non-Linear Mech. 115, 11–19. http://dx.doi.org/10.1016/j.ijnonlinmec.2019.05.001.

Cao, Y., Hutchinson, J.W., 2012a. From wrinkles to creases in elastomers: the instability and imperfection-sensitivity of wrinkling. Proc. R. Soc. A: Math. Phys. Eng. Sci. 468 (2137), 94–115. http://dx.doi.org/10.1098/rspa.2011.0384.

Cao, Y., Hutchinson, J.W., 2012b. Wrinkling phenomena in Neo-Hookean film/substrate bilayers. J. Appl. Mech. 79 (3), 031019. http://dx.doi.org/10.1115/1.4005960.

Chansoria, P., Blackwell, J., Etter, E.L., Bonacquisti, E.E., Jasiewicz, N., Neal, T., Kamal, S.A., Hoque, J., Varghese, S., Egan, T., Nguyen, J., 2022. Rationally designed anisotropic and auxetic hydrogel patches for adaptation to dynamic organs. Adv. Funct. Mater. 32 (43), 2207590. http://dx.doi.org/10.1002/adfm.202207590.

Chen, X., Hutchinson, J.W., 2004. Herringbone buckling patterns of compressed thin films on compliant substrates. J. Appl. Mech. 71 (5), 597–603. http://dx.doi.org/10.1115/1.1756141.
Choi, J.B., Lakes, R.S., 1992. Non-linear properties of metallic cellular materials with a negative Poisson's ratio. J. Mater. Sci. 27 (19), 5375–5381. http://dx.doi.org/10.1007/BF02403846.
Choi, W., Song, J., Khang, D.-Y., Jiang, H., Huang, Y., Rogers, J., 2007. Biaxially stretchable "wavy" silicon nanomembranes. Nano Lett. 7, 1655–1663. http://dx.doi.org/10.1021/nl0706244.
Chung, J.Y., Nolte, A.J., Stafford, C.M., 2011. Surface wrinkling: A versatile platform for measuring thin-film properties. Adv. Mater. 23 (3), 349–368. http://dx.doi.org/10.1002/adma.201001759.
Ciambella, J., Saccomandi, G., 2014. A continuum hyperelastic model for auxetic materials. Proc. R. Soc. A: Math. Phys. Eng. Sci. 470 (2163), 20130691. http://dx.doi.org/10.1098/rspa.2013.0691.
Crespo, J., Montáns, F.J., 2018. A continuum approach for the large strain finite element analysis of auxetic materials. Int. J. Mech. Sci. 135, 441–457. http://dx.doi.org/10.1016/j.ijmecsci.2017.11.038.
Crosby, A.J., 2010. Why should we care about buckling? Soft Matter 6, http://dx.doi.org/10.1039/C0SM90040K, 5660–5660.
Cutolo, A., Pagliarulo, V., Merola, F., Coppola, S., Ferraro, P., Fraldi, M., 2020. Wrinkling prediction, formation and evolution in thin films adhering on polymeric substrata. Mater. Des. 187, 108314. http://dx.doi.org/10.1016/j.matdes.2019.108314.
Danesh, H., Di Lorenzo, D., Chinesta, F., Reese, S., Brepols, T., 2024. FFT-based surrogate modeling of auxetic metamaterials with real-time prediction of effective elastic properties and swift inverse design. Mater. Des. 248, 113491. http://dx.doi.org/10.1016/j.matdes.2024.113491.
Dolla, W.J.S., Fricke, B.A., Becker, B.R., 2006. Structural and drug diffusion models of conventional and auxetic drug-eluting stents. J. Med. Devices 1 (1), 47–55. http://dx.doi.org/10.1115/1.2355691.
Dorris, J.F., Nemat-Nasser, S., 1980. Instability of a layer on a half space. J. Appl. Mech. 47 (2), 304–312. http://dx.doi.org/10.1115/1.3153660.
Efimenko, K., Rackaitis, M., Manias, E., Vaziri, A., Mahadevan, L., Genzer, J., 2005. Nested self-similar wrinkling patterns in skins. Nat. Mater. 4 (4), 293–297. http://dx.doi.org/10.1038/nmat1342.
Goriely, A., Ben Amar, M., 2005. Differential growth and instability in elastic shells. Phys. Rev. Lett. 94, 198103. http://dx.doi.org/10.1103/PhysRevLett.94.198103.
Guo, T., Kouznetsova, V., Geers, M., Veroy, K., Rokoš, O., 2025. Reduced-order modeling for second-order computational homogenization with applications to geometrically parameterized elastomeric metamaterials. Internat. J. Numer. Methods Engrg. 126 (1), e7604. http://dx.doi.org/10.1002/nme.7604.
Gupta, V., Chanda, A., 2023. Biomechanical modelling of hierarchical metamaterials for skin grafting. In: Materials for Biomedical Simulation: Design, Development and Characterization. Springer Nature Singapore, Singapore, pp. 71–83. http://dx.doi.org/10.1007/978-981-99-5064-5_4.
Gurtin, M.E., Ian Murdoch, A., 1975. A continuum theory of elastic material surfaces. Arch. Ration. Mech. Anal. 57 (4), 291–323. http://dx.doi.org/10.1007/BF00261375.
Gurtin, M.E., Ian Murdoch, A., 1978. Surface stress in solids. Int. J. Solids Struct. 14 (6), 431–440. http://dx.doi.org/10.1016/0020-7683(78)90008-2.
Harrison, C., Stafford, C.M., Zhang, W., Karim, A., 2004. Sinusoidal phase grating created by a tunably buckled surface. Appl. Phys. Lett. 85 (18), 4016–4018. http://dx.doi.org/10.1063/1.1809281.
Hassani, B., Hinton, E., 1998. A review of homogenization and topology opimization II—analytical and numerical solution of homogenization equations. Comput. Struct. 69 (6), 719–738. http://dx.doi.org/10.1016/S0045-7949(98)00132-1.
Haughton, D., Ogden, R., 1978. On the incremental equations in non-linear elasticity— I. Membrane theory. J. Mech. Phys. Solids 26 (2), 93–110. http://dx.doi.org/10.1016/0022-5096(78)90016-9.
Hong, W., Zhao, X., Suo, Z., 2009. Formation of creases on the surfaces of elastomers and gels. Appl. Phys. Lett. 95, http://dx.doi.org/10.1063/1.3211917.
Huang, Z., Hong, W., Suo, Z., 2005. Nonlinear analyses of wrinkles in a film bonded to a compliant substrate. J. Mech. Phys. Solids 53 (9), 2101–2118. http://dx.doi.org/10.1016/j.jmps.2005.03.007.
Huang, J., Juszkiewicz, M., de Jeu, W.H., Cerda, E., Emrick, T., Menon, N., Russell, T.P., 2007. Capillary wrinkling of floating thin polymer films. Science 317 (5838), 650–653. http://dx.doi.org/10.1126/science.1144616.
Huang, C., Tang, S., Peng, X., 2017. Study of surface instability about hyperleastic films on auxetic subsrtates under compression. Chin. J. Theor. Appl. Mech. 49 (4), 758–762. http://dx.doi.org/10.6052/0459-1879-17-161.
Hutchinson, J.W., 2013. The role of nonlinear substrate elasticity in the wrinkling of thin films. Philos. Trans. R. Soc. A: Math. Phys. Eng. Sci. 371 (1993), 20120422. http://dx.doi.org/10.1098/rsta.2012.0422.
Khang, D.-Y., Jiang, H., Huang, Y., Rogers, J.A., 2006. A stretchable form of single-crystal silicon for high-performance electronics on rubber substrates. Science 311 (5758), 208–212. http://dx.doi.org/10.1126/science.1121401.
Kolken, H.M., Janbaz, S., Leeflang, S.M., Lietaert, K., Weinans, H.H., Zadpoor, A.A., 2018. Rationally designed meta-implants: A combination of auxetic and conventional meta-biomaterials. Mater. Horizons 5 (1), 28–35. http://dx.doi.org/10.1039/C7MH00699C.
Lakes, R., 1987. Foam structures with a negative Poisson's ratio. Science 235 (4792), 1038–1040. http://dx.doi.org/10.1126/science.235.4792.1038.
Lakes, R., 1993. Advances in negative Poisson's ratio materials. Adv. Mater. 5 (4), 293–296. http://dx.doi.org/10.1002/adma.19930050416.
Li, H., Cai, S., Zhang, Y., Hwang, K.-C., Ma, Y., Feng, X., 2019. Local wrinkling versus global buckling of stiff film bonded to finite-thick substrate. Extrem. Mech. Lett. 29, 100453. http://dx.doi.org/10.1016/j.eml.2019.100453.
Lin, P.-C., Yang, S., 2009. Mechanically switchable wetting on wrinkled elastomers with dual-scale roughness. Soft Matter 5, 1011–1018. http://dx.doi.org/10.1039/B814145B.
Maraghechi, S., Rokoš, O., Peerlings, R., Geers, M., Hoefnagels, J., 2024. Harvesting deformation modes for micromorphic homogenization from experiments on mechanical metamaterials. Int. J. Solids Struct. 301, 112916. http://dx.doi.org/10.1016/j.ijsolstr.2024.112916.
Milstein, F., Huang, K., 1979. Existence of a negative Poisson ratio in fcc crystals. Phys. Rev. B 19 (4), 2030. http://dx.doi.org/10.1103/PhysRevB.19.2030.
Moulinec, H., Suquet, P., 1998. A numerical method for computing the overall response of nonlinear composites with complex microstructure. Comput. Methods Appl. Mech. Engrg. 157 (1–2), 69–94.
Mueller, S., Kruck, B., Baudisch, P., 2013. LaserOrigami: Laser-cutting 3D objects. In: Proceedings of the SIGCHI Conference on Human Factors in Computing Systems. CHI '13, Association for Computing Machinery, New York, NY, USA, pp. 2585–2592. http://dx.doi.org/10.1145/2470654.2481358.
Nikravesh, S., Ryu, D., Shen, Y.-L., 2019a. Direct numerical simulation of buckling instability of thin films on a compliant substrate. Adv. Mech. Eng. 11 (4), 1687814019840470. http://dx.doi.org/10.1177/1687814019840470.
Nikravesh, S., Ryu, D., Shen, Y.-L., 2019b. Surface instability of composite thin films on compliant substrates: Direct simulation approach. Front. Mater. 6, http://dx.doi.org/10.3389/fmats.2019.00214.
Pamulaparthi Venkata, S., Balbi, V., Destrade, M., Zurlo, G., 2024. Designing necks and wrinkles in inflated auxetic membranes. Int. J. Mech. Sci. 268, 109031. http://dx.doi.org/10.1016/j.ijmecsci.2024.109031.
Popereka, M.Y., Balagurov, V., 1970. Ferromagnetic films having a negative Poisson ratio. Sov. Phys. Solid State 11 (12), 2938–2943.
Shield, T.W., Kim, K.S., Shield, R.T., 1994. The buckling of an elastic layer bonded to an elastic substrate in plane strain. J. Appl. Mech. 61 (2), 231–235. http://dx.doi.org/10.1115/1.2901434.
Song, J., Jiang, H., Liu, Z., Khang, D., Huang, Y., Rogers, J., Lu, C., Koh, C., 2008. Buckling of a stiff thin film on a compliant substrate in large deformation. Int. J. Solids Struct. 45 (10), 3107–3121. http://dx.doi.org/10.1016/j.ijsolstr.2008.01.023.

Stafford, C.M., Guo, S., Harrison, C., Chiang, M.Y.M., 2005. Combinatorial and high-throughput measurements of the modulus of thin polymer films. Rev. Sci. Instrum. 76 (6), 062207. http://dx.doi.org/10.1063/1.1906085.

Stafford, C.M., Harrison, C., Beers, K.L., Karim, A., Amis, E.J., VanLandingham, M.R., Kim, H.-C., Volksen, W., Miller, R.D., Simonyi, E.E., 2004. A buckling-based metrology for measuring the elastic moduli of polymeric thin films. Nat. Mater. 3 (8), 545–550. http://dx.doi.org/10.1038/nmat1175.

Steigmann, D.J., Ogden, R.W., 1997. Plane deformations of elastic solids with intrinsic boundary elasticity. Proc. R. Soc. Lond. Ser. A Math. Phys. Eng. Sci. 453 (1959), 853–877. http://dx.doi.org/10.1098/rspa.1997.0047.

Stoop, N., Lagrange, R., Terwagne, D., Reis, P.M., Dunkel, J., 2015. Curvature-induced symmetry breaking determines elastic surface patterns. Nat. Mater. 14 (3), 337–342. http://dx.doi.org/10.1038/nmat4202.

Sun, S., Brandt, M., Easton, M., 2017. Powder bed fusion processes: An overview. Laser Addit. Manuf. 55–77. http://dx.doi.org/10.1016/B978-0-08-100433-3.00002-6.

Taylor, R.L., 2014. FEAP-A finite element analysis program.

Timoshenko, S., 1983. History of Strength of Materials: With a Brief Account of the History of Theory of Elasticity and Theory of Structures. Dover Publications, New York.

Timoshenko, S., Woinowsky-Krieger, S., et al., 1959. Theory of Plates and Shells. 2, McGraw-Hill, New York.

Venkata, S.P., Balbi, V., Destrade, M., Accoto, D., Zurlo, G., 2023. Programmable wrinkling for functionally-graded auxetic circular membranes. Extrem. Mech. Lett. 63, 102045. http://dx.doi.org/10.1016/j.eml.2023.102045.

Volynskii, A.L., Bazhenov, S., Lebedeva, O.V., Bakeev, N.F., 2000. Mechanical buckling instability of thin coatings deposited on soft polymer substrates. J. Mater. Sci. 35 (3), 547–554. http://dx.doi.org/10.1023/A:1004707906821.

Wagner, S., Lacour, S.P., Jones, J., hui I. Hsu, P., Sturm, J.C., Li, T., Suo, Z., 2004. Electronic skin: architecture and components. Phys. E: Low- Dimens. Syst. Nanostructures 25 (2), 326–334. http://dx.doi.org/10.1016/j.physe.2004.06.032.

Wojciechowski, K., Brańka, A., 1989. Negative Poisson ratio in a two-dimensional “isotropic”solid. Phys. Rev. A 40 (12), 7222. http://dx.doi.org/10.1103/physreva.40.7222.

Wolfram Research Inc., 2022. Mathematica, Version 13.1, Champaign, IL. Wolfram Research, Inc., URL: https://www.wolfram.com/mathematica.

Yin, S.-F., Li, B., Cao, Y.-P., Feng, X.-Q., 2018. Surface wrinkling of anisotropic films bonded on a compliant substrate. Int. J. Solids Struct. 141–142, 219–231. http://dx.doi.org/10.1016/j.ijsolstr.2018.02.024.

Zahoor, Y., De Breuker, R., Voskuijl, M., 2020. Preliminary design of a TE morphing surface for rotorcraft. In: AIAA Scitech 2020 Forum. p. 1301.

Zhang, J., Li, Y., Xing, Y., 2019. Theoretical and experimental investigations of transient thermo-mechanical analysis on flexible electronic devices. Int. J. Mech. Sci. 160, 192–199. http://dx.doi.org/10.1016/j.ijmecsci.2019.04.041.

Zhao, Q., Wang, J., Cui, H., Chen, H., Wang, Y., Du, X., 2018. Programmed shape-morphing scaffolds enabling facile 3D endothelialization. Adv. Funct. Mater. 28 (29), 1801027. http://dx.doi.org/10.1002/adfm.201801027.

Zheng, L., Kumar, S., Kochmann, D.M., 2021. Data-driven topology optimization of spinodoid metamaterials with seamlessly tunable anisotropy. Comput. Methods Appl. Mech. Engrg. 383, 113894. http://dx.doi.org/10.1016/j.cma.2021.113894.

Zhuo, L., Zhang, Y., 2015. From period-doubling to folding in stiff film/soft substrate system: The role of substrate nonlinearity. Int. J. Non-Linear Mech. 76, 1–7. http://dx.doi.org/10.1016/j.ijnonlinmec.2015.05.002.